CHEMISTRY OF MATERIALS

Article

pubs.acs.org/cm

Synthesis of Rutile-Phase $Sn_xTi_{1-x}O_2$ Solid-Solution and $(SnO_2)_x/(TiO_2)_{1-x}$ Core/Shell Nanoparticles with Tunable Lattice Constants and Controlled Morphologies

Lena Trotochaud and Shannon W. Boettcher*

Department of Chemistry, The Materials Science Institute, Oregon Nanoscience and Microtechnologies Institute, University of Oregon, Eugene, Oregon 97403, United States

Supporting Information

ABSTRACT: We report the solvothermal synthesis of $Sn_xTi_{1-x}O_2$ solid-solution and $(SnO_2)_x/(TiO_2)_{1-x}$ core/shell nanoparticles with tunable lattice parameters and morphologies over the range of $0 \leq x \leq 1$. The products are characterized by transmission electron microscopy, powder X-ray diffraction, and solid-state nuclear magnetic resonance spectroscopy. Rutile-phase particles with solid-solution or core/shell architectures are synthesized by combining titanium isopropoxide [Ti(O-*i*-Pr)$_4$] with Sn-containing precursors ($SnCl_4$ or SnO_2 nanoparticles, respectively) to favor rutile crystal growth over the typically observed anatase-phase TiO_2. The transition from the anatase to the rutile TiO_2 phase is associated with increasing concentration of the Sn precursor. In the first case, we propose that the mixing of molecular Ti(O-*i*-Pr)$_4$ and $SnCl_4$ precursors leads to the formation of a $Sn_xTi_{1-x}O_2$ solid solution which preferentially crystallizes in the rutile phase due to thermodynamics. In the second case, we propose that the rutile SnO_2 nanoparticles act as nucleation sites for the heteroepitaxial growth of rutile TiO_2, lowering the energy barrier for particle growth and generating $(SnO_2)_x/(TiO_2)_{1-x}$ core/shell particles. The particle morphology and polydispersity are also altered systematically by varying the Ti/Sn ratio of the reactants, with particle elongation normal to the [110] direction observed for higher Sn concentrations. In the absence of Ti precursor, SnO_2 nanowires with diameters <5 nm are formed from $SnCl_4$ under the reaction conditions.

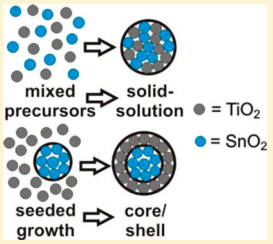

KEYWORDS: *core/shell, solid-solution, nanoparticle, nanowire, solvothermal synthesis, nucleation, titanium dioxide, tin oxide*

1. INTRODUCTION

Mixed-metal oxide nanomaterials are of interest for their applications as gas sensors,[1−4] heterogeneous catalysts and catalyst supports,[4−8] and electrode materials.[7,9−11] In particular, solid solutions of the tin and titanium dioxides, hereafter denoted as $Sn_xTi_{1-x}O_2$, have received attention for their photocatalytic activity for oxidation of organic molecules[12,13] and for their use in dimensionally stable anodes (DSA).[14,15] Our interest in the $Sn_xTi_{1-x}O_2$ system concerns the latter application, with the eventual goal of designing oxide-based electrocatalysts with precise nanostructures where rutile-phase transparent-oxide hosts are coupled with thin shells of highly active, but precious, rutile-phase oxides such as RuO_2 and IrO_2. Precise control is needed in the design and fabrication of such materials if they are to be incorporated into high-performance electrodes.[14,16]

The tunability of nanoparticle (NP) materials involves control of shape, size, composition, and crystal structure. A variety of methods for synthesizing metal oxide and mixed-metal oxide NPs exist that provide varying levels of such control over the reaction products.[17−24] This study involves a fundamental investigation of nanoscale SnO_2−TiO_2 mixed oxides and aims to improve synthetic control over crystal structure and morphology by understanding and manipulating nucleation and growth processes.

TiO_2 is used for dye-sensitized solar cells, and extensive work has been done to investigate the properties of these materials.[25−31] Bulk TiO_2 crystallizes predominantly in the anatase or rutile phases. Solution-based syntheses of TiO_2 NPs largely yield products with the anatase crystal structure.[32−37] In many cases organic capping ligands are effective in controlling the morphologies of anatase TiO_2 NPs by preferentially binding to certain crystal facets, thus inhibiting particle growth along these crystallographic directions.[17,32,36] Few studies, however, report the synthesis of phase-pure rutile TiO_2 NPs.[38−43] Those syntheses that do yield rutile TiO_2 are performed under highly acidic aqueous conditions, making the reactions incompatible with organic stabilizing ligands (which are soluble in organic solvents such as ethanol). Without surface-stabilizing agents, these aqueous reactions yield products that are morphologically ill-defined aggregates of needle or rod-shaped particles.[44−47]

SnO_2 nanostructures have been synthesized by methods including high-temperature thermal oxidation,[48−50] hydrothermal,[51−54] nonaqueous solution,[55−57] and sol−gel[58,59] techniques. SnO_2 crystallizes only in the rutile structure (cassiterite). The majority of reports describing SnO_2 NPs describe morphologies including crystalline nanorods,[51,54,60]

Received: June 18, 2011
Revised: August 31, 2011
Published: October 27, 2011

nanobelts,[49] and nanowires of various aspect ratios with lengths ranging from several[50,53] to hundreds[48,49] of micrometers, and diameters as small as 3.4 nm.[54] These have useful dimensions for gas-sensing applications.[51] Several solution-based methods produce uniform spherical particles less than 5 nm in diameter.[56−58]

Bulk systems of the mixed SnO_2−TiO_2 oxides have been explored previously. Studies on the thermal, electronic, and structural properties of bulk $Sn_xTi_{1-x}O_2$ solid solutions are reported for both theoretical[61−64] and experimental samples prepared by high-temperature solid-state reactions of mixtures of SnO_2 and TiO_2 powders.[65−68] The bulk products of these high-temperature SnO_2−TiO_2 reactions are morphologically ill-defined micropowders.

Reports of $Sn_xTi_{1-x}O_2$ nanoscale systems are few and are largely focused on application of the products to photocatalysis. These solution-based techniques, which include hydrothermal,[69,70] sol−gel,[71] and polyol-mediated[72] methods, provide limited synthetic control over $Sn_xTi_{1-x}O_2$ NP morphology and crystal structure. The transition from anatase to rutile with increased tin-doping has been noted, however the ratio of tin required to complete this transformation seems largely dependent on the particular synthetic method. For example, Zhao et al. recently reported a hydrothermal method in which the pure rutile product was obtained for $Sn_{0.06}Ti_{0.94}O_2$,[69] whereas Asokan et al. synthesize $Sn_{0.5}Ti_{0.5}O_2$ wires that maintain the anatase crystal structure by an electrospinning method.[73] To the best of our knowledge, there have been no reports of nonaqueous growth of $Sn_xTi_{1-x}O_2$ NPs mediated by organic ligands.

Particle composition and morphology has also been controlled through the use of preformed NP seeds as nucleation sites. In aqueous solution, Li et al.[47] used preformed rutile TiO_2 NP seeds (average size = 6.9 nm) to induce the rutile structure in their pure TiO_2 products, although manipulation of reaction time and temperature generated anatase/rutile mixed products in some cases. Qi et al. reported the formation of rutile TiO_2 particles in aqueous solution by addition of $SnCl_2{\cdot}2H_2O$ to the $TiCl_4$ hydrolysis reaction mixture.[74] The authors propose that the SnO_2 nuclei formed during hydrolysis act as heterogeneous nucleation templates for rutile TiO_2 growth. However, the [Sn]/[Ti] molar ratio was varied only up to 0.1, and the particle morphology remains poorly defined and polydisperse. Tao et al. report that nanocrystalline rutile TiO_2 shells form on the surface of wollastonite ($CaSiO_3$) particles in the presence of $SnCl_4$.[75] The anatase-to-rutile phase transition occurs with increasing $SnCl_4$ content and is observable by X-ray diffraction (XRD) analysis. The authors propose that the reactive $SnCl_4$ precursor quickly forms SnO_2, which then induces heterogeneous nucleation of rutile titania, but they did not determine the local environment of the tin atoms in their final products. The SnO_2 NP seeding method has not previously been extended to create mixed-oxide $(SnO_2)_x/(TiO_2)_{1-x}$ core/shell NP structures, nor has the nucleation and growth of these heteroepitaxial NP products been studied in any detail.

Here, we report a study of the solvothermal synthesis of phase-pure rutile nanoparticles containing mixtures of tin and titanium oxides. A key facet of the synthesis is that Sn precursors are introduced into the reaction mixture either as preformed SnO_2 NPs or as a reactive molecular $SnCl_4$ precursor. In the SnO_2 NP seeded-growth method, we hypothesize that using a rutile seed as a template lowers the activation energy for TiO_2 rutile formation by eliminating the energy barrier to nucleation. For the in situ $SnCl_4$ nucleation method, we hypothesize that the presence of the reactive Sn precursor in the initial solution and in the product affects the overall thermodynamics of the reaction, preferencing formation of a Sn/Ti solid-solution rutile product relative to the anatase phase. We show that introducing SnO_2 NP seeds yields products with characteristics consistent with the $(SnO_2)_x/(TiO_2)_{1-x}$ core/shell architecture, while using the molecular $SnCl_4$ precursor generates $Sn_xTi_{1-x}O_2$ solid-solution particles. The products are characterized to reveal insights into the nucleation and growth of these two different SnO_2−TiO_2 mixed-oxide NP architectures. Such understanding is key to the effective design of mixed-oxide nanoscale systems with complex and controlled structure.

2. EXPERIMENTAL SECTION

2.1. Chemicals and Materials. Titanium isopropoxide [Ti(O-*i*-Pr)$_4$]; 97%), oleylamine (OM; 70%, tech. grade), oleic acid (OA; 90%, tech. grade), and tin(IV) chloride ($SnCl_4$; 99%) were obtained from Sigma-Aldrich. Benzyl alcohol (min. 98%) was obtained from EMD. Absolute ethanol (CH_3OH; 200 proof), tetrahydrofuran (THF; ultra pure, BHT stabilized), and cyclohexane (99%) were obtained from Mallinckrodt. All chemicals were used without further purification. All water used in reactions was purified to 18.2 MΩ-cm with a Barnstead Nanopure Analytical ultrapure water system (model D11901). TEM grids (carbon type-B, 200 mesh, copper; ultrathin carbon film on holey carbon support film, 400 mesh, copper) were purchased from Ted Pella. Acid digestion vessels (Parr Instrument Company, vessel number 4744, 45 mL) with PTFE-linears were used for the solvothermal reactions.

2.2. Characterization. Powder X-ray diffraction (XRD) patterns were recorded on a Bruker D8 Discover diffractometer operating at 40 mA and 40 kV using monochromated Cu Kα_1 radiation (λ = 1.541 Å, step size = 0.2 or 0.5°, integration time = 10 or 20 s/step). XRD samples were prepared by mounting washed, air-dried NP powders onto borosilicate glass microscope slides using silicone-based vacuum grease as the mounting agent. For XRD particle size analysis, a silicon powder standard was used to determine the instrumental line broadening (fwhm =0.12° 2θ for the Si (111) reflection). Powder XRD patterns were fit using Fityk[76] software (version 0.9.3). All reflections in the full diffraction patterns were fit to Gaussian functions using the standard nonlinear least-squares Levenberg−Marquardt method. Fitting errors in peak positions were typically less than 0.05° 2θ, even in the case of broad and/or overlapping peaks. Fitting errors for values of peak fwhm were typically less than 0.1° 2θ.

Transmission electron microscopy (TEM) analysis of NP morphology was performed on a FEI Technai G^2 Spirit microscope operating at 120 keV, equipped with an SIS Megaview III CCD camera. Most TEM samples were prepared by dropcasting 4 μL of soluble NP samples (see below) onto TEM grids using a micropipet. The grids were rinsed to remove excess organics by careful submersion in ethanol using self-closing tweezers. To minimize particle aggregation on the grids due to drying effects, some TEM samples were prepared using an aerosol method (see the Supporting Information for aerosol apparatus setup). For TEM particle size data, particle moments (i.e., average diameters accounting for particle anisotropy) were measured manually using ImageJ software. Average sizes are reported $d_{avg,Sn\chi}$ or $d_{avg,sd\chi} = x \pm y$ nm, where x is the average measured particle moment and y is the unbiased standard deviation.

Single pulse (5 μs, 30° pulse; 6 s recycling delay) solid-state ^{119}Sn MAS NMR of selected samples was carried out on a Bruker Avance DSX300 MHz WB NMR spectrometer with ^{119}Sn operating at 111.9 MHz. A Bruker 4 mm double resonance MAS probe along with a 4 mm Zirconia rotor system were used at a spinning speed of 14 kHz. The ^{119}Sn chemical shift was referenced to SnO_2 at −604 ppm relative to the standard $(CH_3)_4Sn$. Solid-state MAS NMR spectra were fit to Gaussian/Lorentzian lineshapes using Dmfit (version 20071105b).[77]

dx.doi.org/10.1021/cm201737x|*Chem. Mater.* 2011, 23, 4920−4930

2.3. Synthesis of SnO_2 NP Seeds. SnO_2 seed NPs were synthesized as reported previously by Ba et al.[56] Briefly, 1 mL (8.8 mmol) of $SnCl_4$ was added dropwise to 20 mL benzyl alcohol with vigorous stirring. The reaction mixture was then heated in a temperature-controlled oil bath at 100 °C for 24 h. The temperature was then increased to 110 °C, which was maintained for an additional 8 h. The resulting white precipitate was collected via centrifugation. A small amount of precipitate was dried in air on a borosilicate glass microscope slide for XRD analysis. The remaining precipitate was dispersed in 20 mL THF, giving a slightly yellow dispersion with a NP seed content of ~33 mg/mL (~0.22 M). This NP seed solution was subsequently used for the seeded growth method. The molarity of the seed solution was confirmed by weighing the product following thermal combustion of organics at 700 °C.

2.4. Synthesis of Core/Shell $(SnO_2)_x/(TiO_2)_{1-x}$ NPs via Seeded Growth. Vigorous stirring was maintained throughout the addition of all chemical reagents. For a typical synthesis, X mmol seeds were measured (based on the calculated molarity of the SnO_2 seed solution) into borosilicate glass test tubes. The THF was allowed to evaporate to near dryness in a fume hood under N_2 gas flow (the solids were left visibly moist to encourage resolubilization). Under vigorous stirring, 3 mmol OA (1.06 mL), 2 mmol OM (0.94 mL), and 10 mmol ethanol (0.58 mL) were added sequentially. Typically, the solution was visibly clear and colorless or very slightly yellow upon sufficient mixing of the reagents. Next, a stoichiometric amount of nanopure water (2 mmol, 36 μL) was added dropwise to the reaction mixture. Addition of water sometimes slightly clouded the solution temporarily. This is minimized by maintaining sufficient stirring during H_2O addition. Then Y mmol $Ti(O\text{-}i\text{-}Pr)_4$ was added dropwise, such that $X + Y = 1$ mmol. Addition of $Ti(O\text{-}i\text{-}Pr)_4$ caused the clear solution to turn a slight yellow color due to the formation of titanium oxocarboxyalkoxide complexes, which has been shown to decrease the hydrolytic susceptibility of the titanium precursor.[78,79] The test tubes were then sealed in Teflon-lined stainless steel autoclaves. The reactions were heated to 180 °C in an electric oven and this temperature was maintained for 18 h. After cooling to room temperature in air, the autoclaves were opened and ~2 mL of ethanol were added to precipitate the NPs from the supernatant. The samples were then homogenized with stirring, and a small amount (3–5 drops) of this unwashed reaction mixture was dissolved in 10 mL of cyclohexane. These solutions were later used for TEM analysis. Samples were typically stable suspensions and somewhat optically scattering. Their dispersibility in organic solution is due to the presence of organic capping ligands at the surface. The stability of the particles in solution is dependent on the washing procedure of the as-prepared samples, with unwashed samples being the most dispersible and staying suspended for weeks, and samples washed with multiple portions of ethanol showing limited solubility and precipitating in as little as 2–3 h.

The remaining reaction mixtures were then centrifuged, washed with ~5 mL of ethanol, dispersed, and centrifuged again. The supernatant was then decanted. This washing procedure was performed three consecutive times. The samples were then dried in air to give powders, which were homogenized for XRD analysis. Selected powder samples were used for solid-state NMR experiments without further treatment. The dried powders were slightly yellow for the pure TiO_2 samples, and sample colors became progressively darker with increasing tin concentration, approaching a brown color for the pure SnO_2 samples. A similar color transition was observed in the postreaction supernatant solutions. Thermal combustion of these supernatant solutions at 700 °C left little (<1 mg) to no residue, implying that the color change is due to partially decomposed ligands and that all inorganic reagents added are incorporated into the NP powder products. The washed, dried powders also lost their color upon heating to 500 °C in air (see Figure S1 in the Supporting Information), suggesting that the color of the products is also due to the presence of partially decomposed ligand impurities.

2.5. $Sn_xTi_{1-x}O_2$ solid-solution NPs via in situ nucleation. The procedure for the in situ nucleation method is similar to that for the seeded-growth method. In place of the THF seed solution, a solution of 0.5 M $SnCl_4$ in ethanol prepared immediately prior to the reaction setup was used as the Sn-containing precursor. Addition of $SnCl_4$ to ethanol was performed in a fume hood, as the resulting reaction is exothermic and immediately releases HCl gas. All other experimental parameters and workup conditions were identical to those described above. Qualitative observations regarding solubility and colors of the reaction products were similar to those for products made by the seeded-growth method.

2.6. Sample Nomenclature. Sample names are differentiated for the two synthesis methods in the following way: χ, defined by χ = mmol Sn/(mmol Sn + mmol Ti), is a number between 0 and 1 indicating the mole fraction of tin-containing precursor in the reaction mixture. The samples are differentiated as Snχ for the in situ $SnCl_4$ nucleation method, and sdχ for the seeded-growth method. For example, Sn0.5 corresponds to a sample prepared using the in situ nucleation method with 0.5 mol fraction of $SnCl_4$, and sd0.2 is a sample prepared using the seeded-growth method with 0.2 mol fraction of SnO_2 NP seeds.

3. RESULTS

3.1. Powder XRD. Wide-angle XRD patterns were collected to determine the crystal structures and lattice constants of the products and are shown in Figure 1. Data

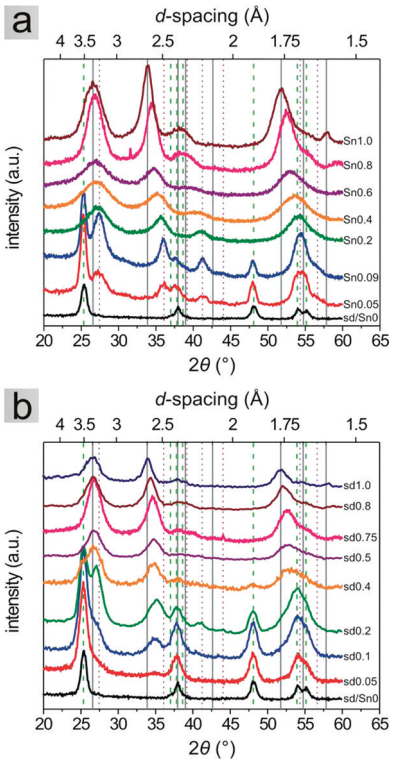

Figure 1. Powder XRD patterns for SnO_2–TiO_2 mixed-oxide samples obtained from the in situ nucleation method (a) and the seeded-growth method (b). Vertical reference lines for anatase TiO_2 (dash), rutile TiO_2 (dot), and rutile SnO_2 (solid) reflections are included as a guide for the eye. Intensity units are arbitrary and the data sets have been offset vertically to show the evolution of the powder patterns with increasing tin concentration. Patterns have been smoothed by 3-point adjacent-averaging but are not background corrected.

from the XRD analysis for selected diffraction reflections for all samples is summarized in Table S1 in the Supporting Information. Values for d-spacings were calculated from the fitted peak positions and based on the Bragg condition for reflection ($d = \lambda/2\sin\theta$). For samples containing both the anatase and rutile phases, the mass fraction of rutile is estimated

dx.doi.org/10.1021/cm201737x | Chem. Mater. 2011, 23, 4920–4930

from:

$$W_R = I_R/(0.886I_A + I_R) \quad (1)$$

where W_R is the mass fraction of rutile, 0.886 is a unit-less correction factor to account for the differences in scattering intensities due to the different crystal structures, and I_A and I_R are the integrated intensities of the anatase (101) and the rutile (110) reflections, respectively.[80]

3.1.1. In situ $SnCl_4$ Nucleation Method. The Sn precursor content was varied from 0 to 100 mol %, while the total inorganic precursor amount was held constant at 1 mmol. In the absence of Sn precursors, the TiO_2 NPs crystallized only in the anatase phase, as evidenced by the single peak near 25.3° 2θ corresponding to the (101) anatase reflection. The onset of a second set of XRD reflections is observed between 2 and 5 mol % $SnCl_4$ (Figure 1a). The peak at 27.3° 2θ corresponds to a rutile (110) reflection near that of pure TiO_2 (27.4° 2θ), and all other reflections in this set can also be indexed to the rutile phase. The rutile reflections increase in intensity relative to anatase reflections with increasing $SnCl_4$ concentration. The positions of the rutile reflections undergo a shift to lower 2θ with increasing $SnCl_4$ concentration, approaching the expected values for pure SnO_2. Reflections indicating the presence of anatase in the products are absent for $SnCl_4$ concentrations exceeding 15%.

3.1.2. Seeded-Growth Method. The powder XRD patterns for SnO_2–TiO_2 mixed-oxide samples prepared by the seeded-growth method are different from those of the in situ nucleation method (Figure 1b). When no SnO_2 seeds are present in the reaction mixture, only reflections corresponding to anatase TiO_2 are observed in the XRD pattern. A decrease in intensity of the anatase reflections is observed with increasing SnO_2 seed concentration. Rutile reflections are first observed for products synthesized with 3–5% seeds. Unlike the in situ nucleation method, the rutile (110) reflection appears at ~27° 2θ, which is intermediate to that of the pure TiO_2 (27.4° 2θ) and pure SnO_2 (26.6° 2θ) positions. The positions of the rutile reflections shift to lower 2θ with increasing seed concentration, and continue to approach the expected values for pure SnO_2. Reflections corresponding to the anatase phase are observed only for samples synthesized with SnO_2 seed concentrations less than 50%.

3.1.4. Particle Size Analysis from XRD. Particle size was estimated from the XRD patterns using the Scherrer equation:

$$D = \frac{K\lambda}{\beta \cos\theta} \quad (2)$$

where D is the average particle diameter, K is the dimensionless particle shape factor, λ is the wavelength of the incident X-rays, β is the fwhm of the Bragg reflection in radians (corrected for instrumental broadening), and cos θ is the position of the Bragg reflection in degrees θ (2θ/2). The value of K depends on the morphologies of the particles measured; we use a K value of 0.9, which is the value typically used for spherical particles or as an estimation of K when the sample morphology is unknown or polymorphic. Particle sizes were calculated from all reflections between 20 and 60° 2θ. Figure 2 summarizes the particle sizes calculated for the anatase (101) and the rutile (110) and (101) reflections. The calculated particle sizes are also presented in Table S1 in the Supporting Information. Differences in particle sizes extracted from different Bragg peaks are indicative of anisotropic particle shapes. This topic will be addressed further in the discussion section. Uncertainties in particle sizes from the Scherrer equation can arise from peak fitting (in the peak position and fwhm) and the chosen value of K. In our case, the latter of these is presumed to dominate, as uncertainties in β and θ from peak fitting are small (typically ±0.1° 2θ and ±0.05° 2θ, respectively). We also note that the Scherrer equation provides the mean size of crystalline domains in the sample along the particular crystallographic axis, which may be smaller than the particle size. In other words, the Scherrer equation gives a lower limit of particle size if the particles consist of multiple grains. Here, TEM imaging of the products formed from both $SnCl_4$ and SnO_2 NP precursors show lattice fringes that are continuous over entire particles (Figure 3, insets), indicating that the particles are single grain. In accord with this finding, the particle sizes determined via the Scherrer analysis of the powder XRD patterns agree with those determined by TEM analysis within the error estimates of each measurement (Figure 2).

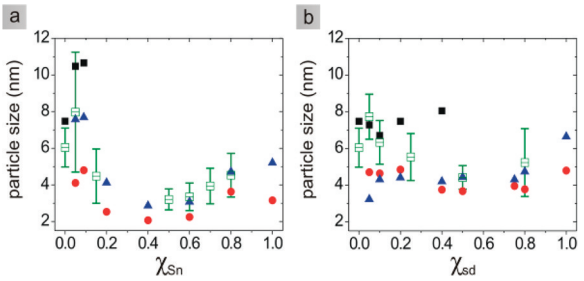

Figure 2. Particle sizes calculated from XRD reflections using the Scherrer equation and TEM images for (a) the in situ nucleation method and (b) the seeded growth method. Open symbols with error bars represent data obtained from TEM analysis. Each set of solid symbols represents data obtained from a different XRD reflection as follows: squares = anatase (101); circles = rutile (110); triangles = rutile (101). The same XRD data is presented in numerical form in Table S1 in the Supporting Information.

Nonuniform strain in the crystal lattice can also contribute to peak broadening. Williamson–Hall plots are typically used to deconvolute broadening due to particle strain from that due to size.[81] However, even for large values of strain, the magnitude of peak broadening is less than that caused by small (<10 nm) particle size.[82] For such small particles, size broadening dominates, especially because the lattice mismatch between the rutile TiO_2 and SnO_2 is relatively small. As expected, Williamson–Hall plots generated for select samples did not provide meaningful analyses, and thus the particle sizes we obtain from XRD patterns were not corrected for nonuniform strain.

3.2. Transmission Electron Microscopy Analysis. As expected for high-temperature solvothermal reaction conditions,[32,78] TEM analysis shows that all products of both synthetic methods were crystalline with no evidence of amorphous material. The absence of amorphous material in the nanoparticle powder products was confirmed by differential scanning calorimetry experiments, where exothermic peaks associated with crystallization were not observed for the nanoparticle samples (see Figure S2 in the Supporting Information).

3.2.1. Seeded-Growth Method. The morphologies of the particles were analyzed using TEM imaging (Figure 3). Particle sizes as determined by TEM imaging are included in Figure 2 (see the Supporting Information for complete particle-size-

dx.doi.org/10.1021/cm201737x|Chem. Mater. 2011, 23, 4920–4930

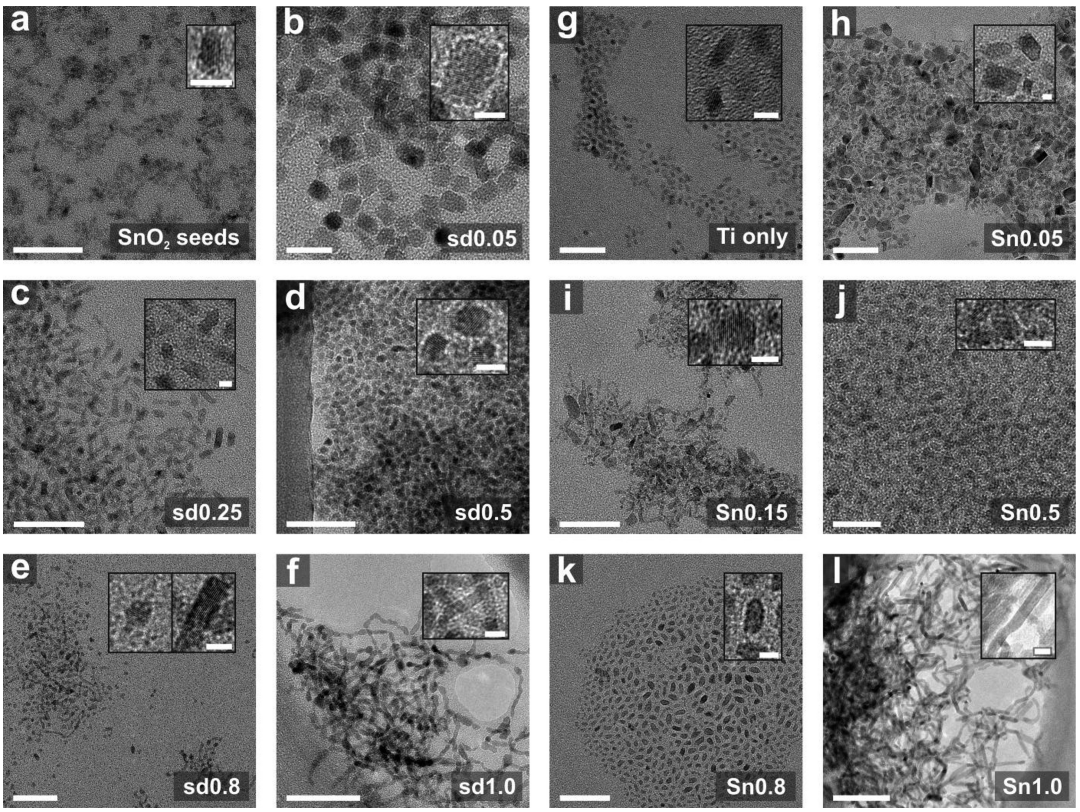

Figure 3. Representative TEM images for samples prepared using (b–f) the seeded-growth method and (h–l) the in situ $SnCl_4$ nucleation method. The (a) as-synthesized SnO_2 NP seeds and (g) pure TiO_2 NPs (sd/Sn0) are included for comparison. Large scale bars indicate 50 nm for all images. Scale bars are 5 nm for the insets, which show continuous lattice fringes across the particles.

distribution histograms). The SnO_2 seeds initially are ellipsoids (Figure 3a), which is consistent with the reports of Ba et al.[56] The pure anatase TiO_2 particles synthesized in the absence of Sn precursors (Figure 3g) appear relatively monodisperse with $d_{avg,sd/Sn0}$ = 6.0 ± 1.1 nm. Lattice fringes corresponding to the anatase (101) planes (d-spacing = 3.51 Å) are visible with an average measured length of 3.6 ± 0.1 Å. Addition of 5 mol % SnO_2 seeds drastically alters the morphology of the anatase particles (Figure 3b), which increase in size to $d_{avg,sd0.05}$ = 7.7 ± 1.2 nm. TEM images show rectangular shapes that are 2D projections of the cuboidal 3D shape of the particles. Analysis of the anatase lattice fringes (average length = 3.6 ± 0.1 Å) reveals that the anisotropy of these particles is orthogonal to the [101] direction. A small population of particles in this sample were identified as SnO_2, based on lattice fringe measurements (3.34 ± 0.03 Å) of the SnO_2 rutile (110) planes (d-spacing = 3.35 Å). Further increasing the seed concentration to χ_{sd} = 0.25 yields mixed-phase samples (Figure 3c) with smaller average particle size, but still a high level of polydispersity ($d_{avg,sd0.25}$ = 5.5 ± 1.3 nm). At χ_{sd} = 0.5, the nanoparticles are uniformly faceted, with the TEM projections appearing as rounded squares (Figure 3d). These particles have a narrower size distribution than all samples with lower χ_{sd} ($d_{avg,sd0.5}$ = 4.4 ± 0.7 nm) and appear highly crystalline in TEM images (Figure 3d inset). At this seed concentration, anatase reflections are no longer detectable in the X-ray diffraction pattern (see above). In the χ_{sd} = 0.8 sample, ($d_{avg,sd0.8}$ = 5.2 ± 1.9 nm) most of the particles appear similar to those for χ_{sd} = 0.5 (Figure 3e). Another small population of elongated rod units is also observed in this sd0.8 sample, which may be products of growth by an oriented attachment mechanism, as is discussed below. Lattice fringe measurements yield an average spacing of 3.4 ± 0.1 Å, which is consistent with the d-spacing calculated for the sd0.8 sample (3.35 Å) from the rutile (110) reflection in the powder XRD pattern. This result indicates that the rods are elongated orthogonal to the [110] direction. The χ_{sd} = 1.0 sample (Figure 3f), in which SnO_2 NP seeds were reacted only with ligands [i.e., no $Ti(O\text{-}i\text{-}Pr)_4$], shows elongated, necklace-like chains markedly different from the as-synthesized seed particles, indicating that the reaction conditions induce restructuring/fusion of the SnO_2 seeds. The fused structures are also crystalline, as is evidenced by the presence of lattice fringes in all the TEM images. All observed lattice fringes indicate preferential particle elongation/fusion occurring orthogonal to the rutile [110] direction.

3.2.2. In situ Nucleation Method. Samples synthesized from molecular $SnCl_4$ and $Ti(O\text{-}i\text{-}Pr)_4$ precursors were also imaged. The χ_{Sn} = 0.05 sample (Figure 3h) is polydisperse ($d_{avg,Sn0.05}$ = 8.0 ± 3.3 nm) with larger prismatic anatase particles visible amid a mass of smaller particles. The χ_{Sn} = 0.15 sample (Figure 3i) is also polydisperse, but with a smaller average particle size and standard deviation ($d_{avg,Sn0.15}$ = 4.5 ± 1.5 nm). Lattice fringes measured for this sample can be attributed to both the TiO_2 anatase (101) and rutile (110) sets of planes, which is consistent with the appearance of both sets of reflections in the XRD pattern. At χ_{Sn} = 0.5 (Figure 3j), particles with less well-defined facets and increased monodispersity with the rutile structure are observed ($d_{avg,Sn0.5}$ = 3.2 ± 0.6 nm). At χ_{Sn} = 0.8 (Figure 3k), some of the particles begin to elongate, increasing polydispersity ($d_{avg,Sn0.8}$ = 4.5 ± 1.2 nm). Imaging of the lattice fringes of the rutile (110) planes indicate particle elongation orthogonal to the [110] direction. In the

dx.doi.org/10.1021/cm201737x|*Chem. Mater.* 2011, 23, 4920–4930

absence of Ti-containing precursor (χ_{Sn} = 1.0), SnO_2 wires are formed (Figure 3l). The average wire diameter was measured to be 3.4 ± 0.6 nm. The average wire length is difficult to determine because of agglomeration on the TEM grid. Lattice fringes measured for the crystalline SnO_2 wires indicate wire growth orthogonal to the [110] direction.

3.3. Solid-State ^{119}Sn MAS NMR. Solid-state ^{119}Sn magic angle spinning (MAS) NMR spectra were collected for the as-prepared sd0.5 and Sn0.5 mixed-oxide samples, and for a pure SnO_2 NP sample (Sn1.0). The normalized spectra are shown in Figure 4. For each spectrum, the total fitted peak area was normalized to one and the relative peak areas were determined.

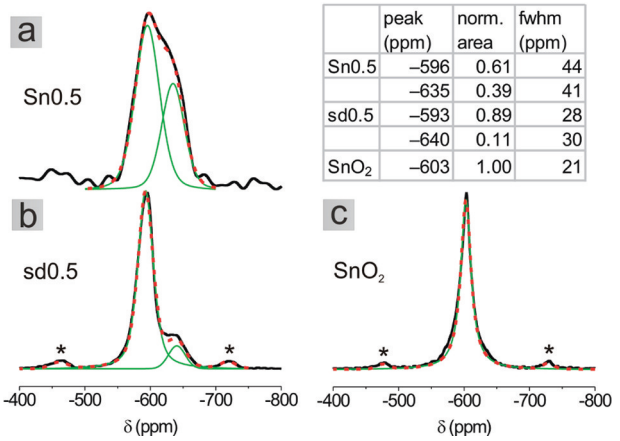

	peak (ppm)	norm. area	fwhm (ppm)
Sn0.5	−596	0.61	44
	−635	0.39	41
sd0.5	−593	0.89	28
	−640	0.11	30
SnO_2	−603	1.00	21

Figure 4. Solid-state MAS NMR spectra of Sn0.5, sd0.5, and SnO_2 nanoparticle powders. Black lines are the intensity normalized spectra, green lines show the ^{119}Sn resonance fits, and red dashed lines give the sums of the peak fits. Stars indicate the MAS spinning side bands (individual fits not shown, but are included in red sums of peak fits).

The pure SnO_2 sample (Figure 4c) shows one ^{119}Sn resonance at −603 ppm, which is consistent with the reference value for pure SnO_2 powder (−604 ppm). The Sn0.5 spectrum (Figure 4a) is fit well by two peaks, one at −596 ppm with a normalized area of 0.61, and another at −635 ppm with an area of 0.39. The sd0.5 sample (Figure 4b) is also fit well by two peaks at −593 and −640 ppm with normalized areas of 0.89 and 0.11, respectively.

4. DISCUSSION

The experimental results are discussed in the context of three main points. First, the morphologies and crystal structures of the SnO_2, TiO_2, and SnO_2−TiO_2 mixed-oxide products are compared to relevant previous work. Second, structural models are proposed and discussed for the SnO_2−TiO_2 mixed-oxide NP products based on experimental data for each of the synthetic methods. For the seeded-growth method, a case is presented for the formation of NPs with a core/shell architecture, compared with solid-solution NP formation in the $SnCl_4$ in situ method. Third, mechanisms of particle nucleation and growth under the two synthetic conditions are discussed in light of the structural models proposed.

4.1. Comparison to Previous Work: TiO_2, SnO_2, and SnO_2−TiO_2 Mixed-Oxide Products. The solvothermal synthesis procedure employed here is a modified version of that reported by Dinh et al. for anatase phase-pure TiO_2 NPs.[32] For the same molar ratios of Ti:OA:OM (1:3:2), Dinh et al. obtain elongated dog-bone shaped particles that appear to be approximately four times larger and are more highly faceted than particles synthesized here. Low magnification images of their particles show a polydisperse sample. As discussed previously, slight changes in reaction conditions have been shown to markedly affect the morphologies of TiO_2 NPs. The two differences between our synthesis and that of Dinh et al. are the method of water introduction to the reaction mixture (direct vs azeotropic vapor phase, respectively) and the Ti-containing alkoxide used (isopropoxide vs *n*-butoxide, respectively), which were both altered in our case for convenience. Ti(O-*i*-Pr)$_4$ is complexed with oleic acid during initial mixing of the precursors, as evidenced by the change from colorless to a yellow solution. The formation of these titanium oxocarboxyalkoxide complexes has been shown to significantly reduce the susceptibility of the titanium precursor to hydrolysis.[78,79] Dinh et al. suggest that the rate of hydrolysis of the Ti precursor influences particle size, with more available water enabling faster hydrolysis and the growth of larger particles. By adding water (36 μL) directly to the reaction mixture, we form smaller anatase TiO_2 NPs, which is contrary to what the report of Dinh et al. would predict. Our results suggest that faster initial hydrolysis forms smaller particles, likely as a result of an increased driving force for nucleation. The nature of the alkoxide group on the metal center will also affect the rate of hydrolysis, with the bulky isopropoxide expected to hinder access to the metal center by water relative to that of the straight-chain butoxide. Additionally, the nuclearity of the metal oxide clusters formed from titanium alkoxides has been shown to be influenced by the alkoxide group.[83,84] Determining which of these experimental factors dominates the hydrolysis pathway requires further experimentation.

Without the addition of Ti precursors in the $SnCl_4$ in situ method, SnO_2 nanowires are obtained which, to the best of our knowledge, are the first obtained using a solvothermal organic ligand-mediated method. While agglomeration of the nanowires on the TEM grid make it difficult to estimate the wire length, the wire diameters (d_{avg} = 3.4 ± 0.6) approach the lower limits (3.4 nm − 4 nm) of those reported for wires and rods synthesized by other solution-based methods.[51,54] The ease and scalability of this synthetic method (our typical ∼4 mL total volume synthesis provides ∼0.5 g of material), along with the small resulting wire diameters, may make it of interest for a variety of applications, particularly sensing.[51] Current efforts include incorporating electronic dopants (e.g., F, Sb) into the SnO_2 nanowires to control conductivity.

Additionally, this work appears to be the first report of SnO_2−TiO_2 mixed-oxide nanoparticles prepared by an organic ligand-mediated solvothermal method. The particles are more uniform and have smaller average sizes than those reported for other solution-based methods (Zhao et al. obtain large polydisperse particles with diameters of 8 ± 3 nm for 10% Sn-doping).[69,71] Some of the particles also have unique core/shell geometries, which is discussed below.

4.2. Structure of the SnO_2−TiO_2 Mixed-Oxide NP Products. *4.2.1. Nanoparticle Structure from XRD Analysis.* Analysis of the XRD data can provide information regarding the organization of SnO_2 and TiO_2 in the NP structure. For example, if the oxides form a solid solution, trends in the rutile lattice parameters as a function of the solid-solution composition can be understood on the basis of Végard's law.[85] For a solid solution, Végard's law predicts a linear relationship between lattice parameter and the

dx.doi.org/10.1021/cm201737x|*Chem. Mater.* 2011, 23, 4920–4930

concentrations of the solid-solution components, and is expressed by:

$$a_{AB} = xa_A + (1 - x)a_B \quad (3)$$

Here, a_{AB} is the lattice parameter for the solid solution, a_A and a_B are the lattice parameters of the individual compounds, and x is the mole fraction of component A. Positive deviations from Végard's law (i.e., that the calculated lattice parameter is larger than that predicted by Végard's law) for oxide solid solutions have been documented for a variety of systems,[86−88] including experimental[65,66] and theoretical[62] $Sn_xTi_{1-x}O_2$ solid solutions. Recently, however, Ma and Navrotsky reported a calorimetric study of $Sn_xTi_{1-x}O_2$ solid solutions that obey Végard's law.[67] For the XRD patterns in Figure 1, d-spacings for the rutile (110) and (101) reflections were calculated (see Table S1 in the Supporting Information). Assuming the formation of solid-solution particles that obey Végard's law, theoretical d-spacings for these reflections were calculated from the following relationship for the tetragonal rutile lattice

$$\frac{1}{d^2} = \frac{(h^2 + k^2)}{a^2} + \frac{l^2}{c^2} \quad (4)$$

where a and c are the lattice constants of the solid-solution phase (given by eq 3 based on the amount of Sn-containing precursor in each sample). Figure 5 shows a graphical comparison of the d-spacings based on experimental measurement and those as predicted for an ideal system obeying Végard's law. Deviations of the experimental data from the ideal Végard's law predictions indicate inhomogeneities in the $Sn_xTi_{1-x}O_2$ solid solutions or the influence of lattice strain, such as would be expected due to a $(SnO_2)_x/(TiO_2)_{1-x}$ core/shell structure.

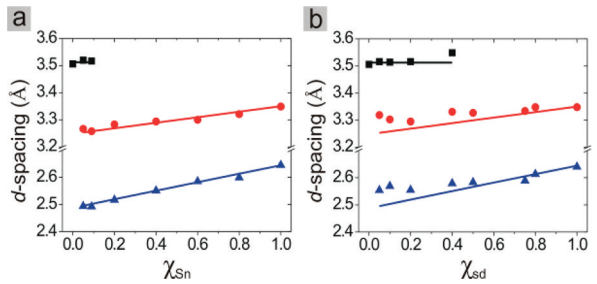

Figure 5. Comparison of experimental data to Végard's law for (a) the in situ nucleation method and (b) the seeded-growth method. Experimental data points (symbols) are plotted on the same axes as ideal Végard's law predictions (lines). Each set of symbols and their corresponding line indicates a different XRD reflection as follows: squares (black) = anatase (101); circles (red) = rutile (110); triangles (blue) = rutile (101). The same data is presented in numerical form in Table S1 in the Supporting Information.

Figure 5a shows that rutile samples from the in situ $SnCl_4$ nucleation method follow Végard's law, indicating the formation of a rutile $Sn_xTi_{1-x}O_2$ solid solution, consistent with our initial hypothesis. These results suggest that Sn is also being incorporated into the anatase phase. The Sn0.05 and Sn0.09 samples contain approximately 42% and 61% weight rutile, respectively, which means that a significant amount of inorganic material crystallizes in the anatase phase for these samples. If the anatase phase contained no SnO_2, we would expect to see positive deviations from Végard's law for the rutile phase in these samples, as the true value of χ_{Sn} for the rutile phase would be higher than expected (i.e., SnO_2 would be concentrated in the rutile phase). Systematic variation in the d-spacing calculated from the anatase (101) reflections is not obvious, however Figure 5a does show a slight increase in the anatase (101) d-spacing for these samples, which could be the result of substitution of larger Sn^{4+} ions into Ti^{4+} lattice positions. A large shift in anatase XRD peak positions is not necessarily expected for low Sn-incorporation, as the anatase crystal structure is less dense than the rutile structure and thus might accommodate Sn^{4+} ions without significant lattice expansion. This is consistent with other reports of Sn-doped anatase TiO_2, where the anatase reflections were found to shift very little, if at all (i.e., the magnitude of the measured shift is within measurement error), with Sn-doping.[69−72,89]

In contrast to NPs obtained from the in situ $SnCl_4$ method, samples obtained from the seeded-growth method (Figure 5b) display a clear positive deviation from Végard's law. For other $Sn_xTi_{1-x}O_2$ systems, some examples of positive deviations from Végard's law have been reported.[65,66] However, in these cases the deviation is positive for all samples in the series, with the magnitude of the deviations smallest near the end points (i.e., at $\chi = 0$ and $\chi = 1.0$) and largest near $\chi = 0.5$ (i.e., with a "bowed" shape). For our samples, the magnitude of deviation is larger for small values of χ_{sd} and gradually decreases as χ_{sd} increases.

We propose that these systematic deviations from Végard's law are due to the formation of particles with a $(SnO_2)_x/(TiO_2)_{1-x}$ core/shell structure. Based on the similarities in lattice constants (SnO_2−TiO_2 fractional lattice mismatch,[90] f_a = 0.03; f_c = 0.07), SnO_2 seeds in solution should serve as a nucleation site for rutile TiO_2 growth. The strain in the crystal lattice caused by a core/shell architecture where there is lattice mismatch has been shown to shift the position of the Bragg reflections toward that of the pure shell material for CdSe/CdS,[91,92] CdS/ZnS,[93] CdSe/ZnS,[94] and InAs/InP[95] core/shell NPs. Dabbousi et al. show that the magnitude of the shift in the Bragg reflection directly correlates to the shell layer thickness, with thicker shells shifting the reflections closer to that of the pure shell material.[94] Likewise, Ghosh et al. show that for very thin shell layers (i.e., $LaPO_4$:Er/Yb core/shell particles with 1 mol % Yb), the magnitude of the shift is small, and in fact closely resembles that expected for a solid-solution system.[96] For our samples, high seed concentrations show the smallest deviations from Végard's law, which is consistent with the formation of thin rutile TiO_2 shells on the rutile SnO_2 seeds. We expect the shells to be thinner at high seed concentrations, as available seed nuclei are abundant compared to the amount of Ti precursor. At low seed concentrations, we expect thicker TiO_2 shells to grow. We therefore expect that a decrease in shell thickness with increasing seed concentration will result in a shift in the rutile reflections toward values for pure SnO_2. The data shown in Figure 5b are consistent with this interpretation. Furthermore, even at the lowest seed concentration where the rutile phase becomes detectable (χ_{sd} = 0.1), the reflection positions do not approach those of pure rutile TiO_2, as is the case in the $SnCl_4$ in situ method. This suggests that even at low seed concentrations, the overall contribution of SnO_2-induced strain on the positions of the rutile reflections is significant.

4.2.2. Solid-State ^{119}Sn MAS NMR as a Probe for Core/Shell vs Solid-Solution Structures. Solid-state NMR provides a probe for local structure. The ^{119}Sn MAS NMR data collected for samples sd0.5, Sn0.5, and Sn1.0 were compared to previous work on $Sn_xTi_{1-x}O_2$ bulk powders to better understand the differences between the NPs obtained by the two methods

dx.doi.org/10.1021/cm201737x|Chem. Mater. 2011, 23, 4920−4930

investigated here. Kulshreshtha et al.[97] studied a series of bulk $Sn_xTi_{1-x}O_2$ ($0.0 \leq x \leq 1.0$) powder samples by ^{119}Sn MAS solid-state NMR and found that with decreasing values of x (i.e., higher Ti content), several additional Sn resonances were observed in the region of $\delta = -630$ to -690 ppm. In pure rutile SnO_2, the Sn^{4+} nuclei are surrounded by ten Sn^{4+} cations as their next-nearest neighbors and one ^{119}Sn resonance is observed in the NMR spectra at $\delta = -604$ ppm. In the mixed-oxide samples, the authors attribute the most intense peaks to those Sn^{4+} nuclei surrounded by ten Sn^{4+} cations as next-nearest neighbors, and the additional lower-intensity peaks at more negative chemical shifts to those Sn^{4+} nuclei with varying numbers of Ti^{4+} as their next-nearest neighbors.

For a constant value of x, we expect to observe significant differences in the ^{119}Sn NMR spectra for particles obtained from the two synthetic methods. For the solid-solution NPs, we expect to observe similar results to those reported for the bulk homogeneous mixtures. For a core/shell NP structure, Sn^{4+} nuclei in the core would still have ten Sn^{4+} next-nearest neighbors, and we expect this peak to have a much larger integrated intensity than that for the Sn^{4+} nuclei close to the core/shell interface or mixed with TiO_2.

For their bulk $Sn_{0.5}Ti_{0.5}O_2$ sample, Kulshreshtha et al. observe two main ^{119}Sn resonances at -591 ppm and -647 ppm, with relative peak areas of 0.62 and 0.38, respectively. As expected, these correspond well to the peak positions (-596 and -635 ppm) and relative areas (0.61 and 0.39) obtained from deconvolution of the $Sn_xTi_{1-x}O_2$ Sn0.5 solid-solution NP sample spectrum (Figure 4a).

The NMR spectrum obtained for the sd0.5 sample (Figure 4b) is different from that for the Sn0.5 sample, and is consistent with a core/shell structure for the sd0.5 particles. The peak positions for the sd0.5 sample (-593 ppm and -640 ppm) are consistent with the $Sn_{0.5}Ti_{0.5}O_2$ sample of Kulshreshtha et al., while the relative areas, now 0.89 and 0.11 respectively, are closer to those determined for the reported bulk $Sn_{0.8}Ti_{0.2}O_2$ sample (relative areas 0.88 and 0.12). We attribute the larger intensity peak to Sn^{4+} in the pure SnO_2 core and the small intensity peak to Sn^{4+} cations at the $(SnO_2)_x/(TiO_2)_{1-x}$ core/shell interface. This interpretation is supported by a simple structural model of an ideal spherical core/shell particle with a diameter of 4.4 nm (equivalent to the average diameter for the sd0.5 samples determined from TEM). For such a particle with an overall composition of $Sn_{0.5}Ti_{0.5}O_2$, we estimate a core diameter of 3.4 nm (which is consistent with the average SnO_2 seed size) and a shell thickness of 0.5 nm (based on the densities and mole fractions of the pure oxides). From this model, we estimate that ~25% of Sn^{4+} atoms would be exposed to the core/shell interface (assuming [100] termination), consistent with the experimental observation that the low intensity ^{119}Sn resonance at -640 ppm in the sd0.5 NMR spectrum is ~20% the intensity of the higher intensity resonance. Additionally, the absence of a set of pure SnO_2 reflections in the XRD pattern is further evidence for the absence of isolated SnO_2 particles (i.e., without a TiO_2 shell). However, we cannot conclusively rule out the possibility of a small degree of mixing of the two oxides in the NP core/shell, which will be discussed below.

4.3. Nucleation and Growth of SnO_2–TiO_2 Mixed-Oxide NPs. *4.3.1. NP Growth/Final Structure As It Relates to Sn-Containing Precursor.* We propose a simple model for the nanoparticle structure obtained from the two synthetic methods, which is shown in Figure 6. In this model, the concentration of the Sn-containing precursor determines the crystal phase of the products, with low initial $\chi_{sd/Sn}$ (i) giving a mixture of anatase and rutile products, and high initial $\chi_{sd/Sn}$ (ii) yielding pure rutile products. Figure 6a shows this model for $Sn_xTi_{1-x}O_2$ solid-solution formation for the in situ nucleation method. The Sn and Ti nuclei are evenly distributed in the reaction mixture, and, at low χ_{Sn}, Sn nuclei are incorporated into both the rutile and anatase phases. The XRD data in Figure 5a are consistent with this model, as the rutile reflections shift in accordance with Végard's law, even for samples rich with anatase.

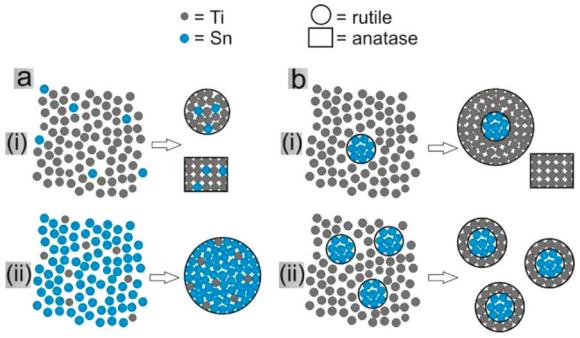

Figure 6. Model depicting nanoparticle structure in (a) the $SnCl_4$ in situ nucleation method and (b) the seeded-growth method, at (i) low and (ii) high Sn precursor concentrations. Further explanation of the figure is contained in the text.

The structural model for the seeded-growth method is shown in Figure 6b. At low seed concentrations, some anatase TiO_2 nucleates and grows, as there are not enough SnO_2 seed nuclei present to accommodate all of the Ti precursor. Above a threshold seed concentration, the amount of available rutile SnO_2 nuclei is sufficient to accommodate all of the Ti precursor, and anatase nucleation ceases. The stability of the seeds under the reaction conditions is a critical factor in determining whether other nucleation and growth processes also occur. If the seeds are stable during the course of the reaction, we expect the sd1.0 sample, i.e. seeds treated solvothermally without $Ti(O\text{-}i\text{-}Pr)_4$, to resemble the as-synthesized seeds. Comparing the TEM images in Figure 3a for the as-synthesized SnO_2 seeds to Figure 3f for the sd1.0 sample, it is clear that significant restructuring of the seeds takes place under the reaction conditions. The TEM images for the sd1.0 sample show beaded structures, where the beads are crystalline and approximately the same size as the as-synthesized seeds. This restructuring is discussed below.

4.3.2. Evidence of NP Restructuring by Oriented Attachment – Implications for the Proposed Growth Model. Figure 7a shows magnified images of three representative crystals from the sd1.0 sample. The lattice fringes, which originate from the rutile (110) set of planes, run the length of the crystals, even across what appear to be kinks in the growing crystal (indicated by arrows in the figure). The irregular morphology of the wires formed in the sd1.0 sample suggests particle fusion by an oriented attachment mechanism. Lee et al. exposed small, spherical SnO_2 NPs to hydrothermal conditions at 200 °C for 24 h and discovered evidence of oriented attachment.[98] The authors showed the formation of elongated and irregularly shaped particles that are similar to our results.

All lattice fringes we measure for these particles indicate anisotropy orthogonal to the [110] direction. Calculations show that the rutile SnO_2 (001) surface is high in energy,

dx.doi.org/10.1021/cm201737x|Chem. Mater. 2011, 23, 4920–4930

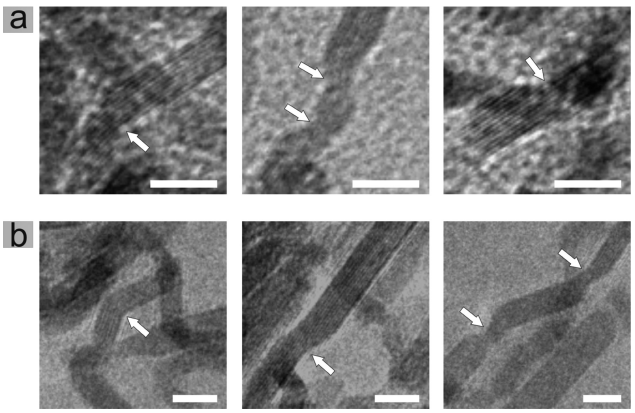

Figure 7. (a) TEM images collected for the sd1.0 sample highlighting three irregularly shaped nanocrystals. Lattice fringes corresponding to the (110) planes are visible along the length of the particles, spanning irregularities in particle shape indicated by white arrows. The sizes of the individual segments of the irregular crystals are on the order of the size of the original SnO_2 NP seeds, suggesting preferential oriented attachment orthogonal to the [110] direction. (b) TEM image of the Sn1.0 sample, also suggesting that oriented attachment is occurring under the reaction conditions. All scale bars are 5 nm in length.

following the trend (110) < (010) < (101) < (001),[64] and SnO_2 wires are known to grow preferentially in this direction.[51,53,54] Thus, oriented attachment along the [001] direction is consistent with our experimental findings.

For comparison, Figure 7b shows three representative particles found in the Sn1.0 sample. The irregular shape of these particles coupled with the single-crystalline structure also suggests that oriented attachment is the mechanism for wire formation under the reaction conditions. This finding implies that the process of SnO_2 nanoparticle nucleation and growth precedes nanowire formation by oriented attachment. Furthermore, observation of oriented attachment in both synthetic methods implies that this growth mechanism occurs after the nucleation process is completed in the seeded-growth method as well. This implies, along with the visible beaded structures, that the SnO_2 NP seeds are not completely dissolved under the reaction conditions.

For the seeded-growth method, the model in Figure 6b describes the extreme case where the SnO_2 NP seeds are completely stable under the reaction conditions. Although all our experimental data for the seeded-growth method support the core/shell hypothesis, we were not able to directly confirm the core/shell structure by TEM.[99] The other extreme is the case where the seeds completely dissolve before any TiO_2 forms. In this case, we would expect a solid solution to form and to observe XRD and ^{119}Sn NMR results for the seeded-growth samples similar, if not identical, to those of the $SnCl_4$ method. This is not consistent with our data. Alternatively, some dissolved SnO_2 could be incorporated into the TiO_2 shell, giving $SnO_2/Sn_xTi_{1-x}O_2$ core/shell NPs where the core is pure SnO_2 and the shell is a solid solution of the two oxides. The data we have collected could be consistent with this situation, and some mixing of the oxides to give a $SnO_2/Sn_xTi_{1-x}O_2$ core/shell structure cannot be conclusively ruled out.

4.3.3. Nucleation of NPs with the Rutile Structure – Kinetic vs Thermodynamic Control. While the models presented in Figure 6 are consistent with the experimental data with respect to the growth and final structure of the NPs, they do not directly address solid-solution versus core/shell particle nucleation. Two possible pathways for NP nucleation are presented schematically in Figure 8. In the first case, we

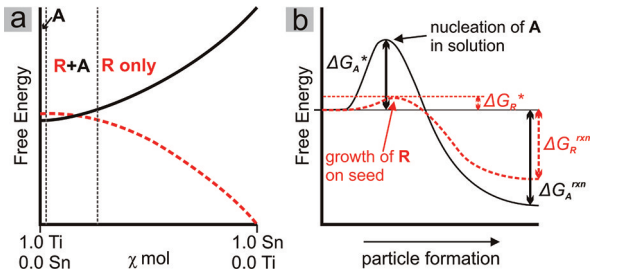

Figure 8. Schematic free energy diagrams for NP nucleation in this study as described in the text. R and A denote rutile and anatase, respectively. (a) Thermodynamic model A for solid-solution NP nucleation. (b) Kinetic model B for seeded nucleation.

consider what we term "thermodynamic Model A" (Figure 8a), where $Sn_xTi_{1-x}O_2$ forms by crystallization of the solid solution. Based on surface energetics and corroborated by experimental data, the pure TiO_2 anatase phase is more stable (i.e., lower energy) for small nanoparticles than the rutile phase.[100] The magnitude of this energy stabilization is likely small, as many methods yield NPs of both phases. For SnO_2, the rutile phase is thermodynamically preferred in both the bulk and the nanoscale regime. For low Sn concentrations, the solid solutions phase segregate, as the relative energies of the anatase and rutile $Sn_xTi_{1-x}O_2$ are likely similar. However, above a certain χ_{Sn}, formation of the anatase phase becomes increasingly energetically unfavorable, and only the rutile phase is observed. Our data for the in situ $SnCl_4$ nucleation method support thermodynamic model A, indicating that the presence of Sn^{4+} in the reaction from the $SnCl_4$ precursor changes the overall thermodynamics of the NP nucleation/growth process.

Alternatively, we also consider a "kinetic model B" (Figure 8b), where particle nucleation (kinetics) controls the final structure. From a classical nucleation and growth perspective, a critical particle size, D^*, must be reached (nucleation) before the particle surface is stable enough to facilitate growth.[101] On a plot of Gibbs free energy, G, vs particle size, the energy required to complete anatase nucleation is given by the activation barrier ΔG_A^*. If $SnCl_4$ reacts more quickly than $Ti(O\text{-}i\text{-}Pr)_4$, small SnO_2 seed clusters could form in situ. The presence of preformed SnO_2 nuclei in solution will lower the activation barrier for particle growth, providing a more kinetically favorable pathway for solid solution formation to occur. Since SnO_2 adopts the rutile structure, the solid solution growing from these nuclei will adopt the rutile structure. Over time, some Ti precursor may inevitably nucleate anatase crystals if inorganic precursors are still available in solution. Anatase nucleation will likely cease above a threshold value of χ_{Sn}, where there are sufficient SnO_2 nuclei to accommodate all of the Ti precursor. Whether or not model B can be conclusively ruled out as the mechanism for the in situ nucleation method will require further investigation.

Model B also applies to the seeded-growth system. The presence of preformed SnO_2 seeds enables heteroepitaxial rutile TiO_2 growth by reducing the energy barrier required for particle nucleation, and thus altering the kinetics of particle growth (cf. Figure 8b) to generate rutile NPs with core/shell architectures. The competing anatase nucleation process is

dx.doi.org/10.1021/cm201737x|*Chem. Mater.* 2011, 23, 4920–4930

more energy intensive than epitaxial rutile shell growth, and if the concentration of seed templates is sufficient, the growth process dominates the nucleation of new particles.

5. CONCLUSIONS

We report the solvothermal synthesis of rutile SnO_2−TiO_2 mixed-oxide nanoparticles by two different methods. By using $SnCl_4$ as the tin-containing precursor, solid-solution $Sn_xTi_{1-x}O_2$ NPs are formed by an in situ nucleation method. For $SnCl_4$ concentrations above $\chi_{Sn} = 0.2$, XRD analysis shows that the products contain only the rutile crystal phase. The anatase to rutile phase transformation correlates with the increasing $SnCl_4$ concentration, and we propose a model for particle growth where Sn^{4+} in the lattice lowers the free energy of the rutile solid solution relative to the anatase phase. Furthermore, by adjusting the $SnCl_4$ concentration, we demonstrate tunability of solid-solution NP morphologies and crystal lattice parameters over the entire region studied ($0 \leq \chi_{Sn} \leq 1$). These well-defined NPs with tunable lattice constants could be useful as scaffolds for growth of more complex nanoscale materials, which we are currently investigating. We also report a gram-scale solution-based method for preparation of SnO_2 nanowires with diameters <5 nm that may be useful for applications such as gas sensing. We are currently investigating the integration of these nanowires into surface-attached assemblies for electrochemical applications, as well as the electronic doping of the nanowires for use as high-surface-area transparent conductive metal oxides.

In a related set of experiments, we used preformed SnO_2 NP seeds to generate $(SnO_2)_x/(TiO_2)_{1-x}$ core/shell NPs, whose core/shell structure is supported by XRD, TEM, and solid-state ^{119}Sn NMR experiments. XRD results show a systematic shift of the rutile Bragg reflections to lower 2θ, with positive deviations from Végard's law. By TEM, we observe evidence of oriented attachment of the SnO_2 seeds under the reaction conditions, which demonstrates the stability of the as-prepared seeds during solvothermal treatment. Solid-state ^{119}Sn NMR analysis show significant differences in the spectra for $Sn_{0.5}Ti_{0.5}O_2$ samples prepared by the two methods, supporting the formation of nanoparticles with core/shell architectures in the seeded-growth method.

A fundamental aspect of this study is the demonstration that nanoparticle growth and nucleation in the SnO_2−TiO_2 system can be controlled by changing the method of Sn precursor introduction. These findings have uses in the design of complex oxide-based functional nanoparticles. We demonstrated that organic ligand-mediated syntheses are effective for controlling the morphology of SnO_2−TiO_2 mixed-metal oxide NPs, and the application of this synthetic method in other mixed-metal oxide systems should be possible.

■ ASSOCIATED CONTENT

Ⓢ Supporting Information

Images of nanoparticle powders, DSC traces, a description of aerosol TEM sample preparation apparatus, and particle-size-distribution histograms. This material is available free of charge via the Internet at http://pubs.acs.org.

■ AUTHOR INFORMATION

Corresponding Author

*E-mail: swb@uoregon.edu.

■ ACKNOWLEDGMENTS

This research was supported by startup funds provided by the University of Oregon and the Oregon Nanoscience and Microtechnologies Institute (ONAMI). Additional support from the Office of Naval Research, through ONAMI is also acknowledged. The authors thank Dr. Jerry Hu of the Materials Research Lab at the University of California, Santa Barbara for collection of, and discussions regarding, solid-state ^{119}Sn NMR data. Support for the NMR facilities is from the National Science Foundation under grant number DMR05-20415. We thank Dr. Sujing Xie and Kurt Langworthy in the Lorry I. Lokey Laboratories for assistance with TEM experiments. The TEM facility is supported in grants from the W.M Keck Foundation, the M.J. Murdock Charitable Trust, ONAMI, the Air Force Research Laboratory (under agreement FA8650-05-1-5041), and the University of Oregon.

■ REFERENCES

(1) Eranna, G.; Joshi, B. C.; Runthala, D. P.; Gupta, R. P. *Crit. Rev. Solid State Mater. Sci.* **2004**, *29*, 111.
(2) Zakrzewska, K. *Thin Solid Films* **2001**, *391*, 229.
(3) Kolmakov, A.; Klenov, D. O.; Lilach, Y.; Stemmer, S.; Moskovits, M. *Nano Lett.* **2005**, *5*, 667.
(4) Kolmakov, A.; Chen, X. H.; Moskovits, M. *J. Nanosci. Nanotechnol.* **2008**, *8*, 111.
(5) Li, Y.; Hasin, P.; Wu, Y. *Adv. Mater.* **2010**, *22*, 1926.
(6) Shiju, N. R.; Guliants, V. V. *Appl. Catal., A* **2009**, *356*, 1.
(7) Fernández-García, M.; Martínez-Arias, A.; Hanson, J. C.; Rodriguez, J. A. *Chem. Rev.* **2004**, *104*, 4063.
(8) Jiao, F.; Frei, H. *Energy Environ. Sci.* **2010**, *3*, 1018.
(9) Angelinetta, C.; Trasatti, S.; Atanasoska, L. D.; Minevski, Z. S.; Atanasoski, R. T. *Mater. Chem. Phys.* **1989**, *22*, 231.
(10) Chen, A.; Nigro, S. *J. Phys. Chem. B* **2003**, *107*, 13341.
(11) Chen, X.; Chen, G.; Yue, P. L. *J. Phys. Chem. B* **2001**, *105*, 4623.
(12) Lin, J.; Yu, J. C.; Lo, D.; Lam, S. K. *J. Catal.* **1999**, *183*, 368.
(13) Zhaoliang, Z.; Jun, M.; Xiyao, Y. *Chem. Eng. J.* **2003**, *95*, 15.
(14) Trasatti, S. *Electrochim. Acta* **2000**, *45*, 2377.
(15) Forti, J. C.; Olivi, P.; de Andrade, A. R. *Electrochim. Acta* **2001**, *47*, 913.
(16) Trasatti, S.; Petrii, O. A. *J. Electroanal. Chem.* **1992**, *327*, 353.
(17) Yin, Y.; Alivisatos, A. P. *Nature* **2005**, *437*, 664.
(18) Cushing, B. L.; Kolesnichenko, V. L.; O'Connor, C. J. *Chem. Rev.* **2004**, *104*, 3893.
(19) Gedanken, A. *Ultrason. Sonochem.* **2004**, *11*, 47.
(20) Jana, N. R.; Chen, Y.; Peng, X. *Chem. Mater.* **2004**, *16*, 3931.
(21) Niederberger, M.; Garnweitner, G. *Chem. Eur. J.* **2006**, *12*, 7282.
(22) Pinna, N.; Garnweitner, G.; Antonietti, M.; Niederberger, M. *J. Am. Chem. Soc.* **2005**, *127*, 5608.
(23) Jana, S.; Aksu, Y.; Driess, M. *Dalton Trans.* **2009**, 1516.
(24) Tsaroucha, M.; Aksu, Y.; Irran, E.; Driess, M. *Chem. Mater.* **2011**, *23*, 2428.
(25) Hagfeldt, A.; Grätzel, M. *Acc. Chem. Res.* **2000**, *33*, 269.
(26) Grätzel, M. *J. Photochem. Photobiol., C* **2003**, *4*, 145.
(27) Kay, A.; Grätzel, M. *Sol. Energy Mater. Sol. Cells* **1996**, *44*, 99.
(28) van de Lagemaat, J.; Park, N.-G.; Frank, A. J. *J. Phys. Chem. B* **2000**, *104*, 2044.
(29) Dittrich, T. *Phys. Status Solidi A* **2000**, *182*, 447.
(30) Hore, S.; Vetter, C.; Kern, R.; Smit, H.; Hinsch, A. *Sol. Energy Mater. Sol. Cells* **2006**, *90*, 1176.
(31) Kopidakis, N.; Benkstein, K. D.; van de Lagemaat, J.; Frank, A. J. *J. Phys. Chem. B* **2003**, *107*, 11307.
(32) Dinh, C. T.; Nguyen, T. D.; Kleitz, F.; Do, T. O. *ACS Nano* **2009**, *3*, 3737.
(33) Tang, J.; Redl, F.; Zhu, Y.; Siegrist, T.; Brus, L. E.; Steigerwald, M. L. *Nano Lett.* **2005**, *5*, 543.
(34) Niederberger, M.; Bartl, M. H.; Stucky, G. D. *Chem. Mater.* **2002**, *14*, 4364.

(35) Wu, B. H.; Guo, C. Y.; Zheng, N. F.; Xie, Z. X.; Stucky, G. D. *J. Am. Chem. Soc.* **2008**, *130*, 17563.
(36) Seo, J.-w.; Jun, Y.-w.; Ko, S. J.; Cheon, J. *J. Phys. Chem. B* **2005**, *109*, 5389.
(37) Jensen, G. V.; Bremholm, M.; Lock, N.; Deen, G. R.; Jensen, T. R.; Iversen, B. B.; Niederberger, M.; Pedersen, J. S.; Birkedal, H. *Chem. Mater.* **2010**, *22*, 6044.
(38) Hu, Y.-S.; Kienle, L.; Guo, Y.-G.; Maier, J. *Adv. Mater.* **2006**, *18*, 1421.
(39) Qu, Y.; Li, X.; Li, R.; Yan, H.; Ouyang, X.; Wang, X. *Mater. Res. Bull.* **2008**, *43*, 97.
(40) Chen, R.-F.; Zhang, L.; Wei, Y.; Hou, D.-L. *J. Mater. Sci.* **2007**, *42*, 7141.
(41) Huang, X.; Pan, C. *J. Cryst. Growth* **2007**, *306*, 117.
(42) Nussbaumer, R. J.; Smith, P.; Caseri, W. *J. Nanosci. Nanotechnol.* **2007**, *7*, 2422.
(43) Wang, W.; Gu, B.; Liang, L.; Hamilton, W. A.; Wesolowski, D. J. *J. Phys. Chem. B* **2004**, *108*, 14789.
(44) Cheng, H.; Ma, J.; Zhao, Z.; Qi, L. *Chem. Mater.* **1995**, *7*, 663.
(45) Wu, Y.; Liu, H.-M.; Xu, B.-Q. *Appl. Organomet. Chem.* **2007**, *21*, 146.
(46) Testino, A.; Bellobono, I. R.; Buscaglia, V.; Canevali, C.; D'Arienzo, M.; Polizzi, S.; Scotti, R.; Morazzoni, F. *J. Am. Chem. Soc.* **2007**, *129*, 3564.
(47) Li, Y.; Fan, Y.; Chen, Y. *J. Mater. Chem.* **2002**, *12*, 1387.
(48) Dai, Z. R.; Gole, J. L.; Stout, J. D.; Wang, Z. L. *J. Phys. Chem. B* **2002**, *106*, 1274.
(49) Gao, T.; Wang, T. *Chem. Commun.* **2004**, 2558.
(50) Kim, W.-S.; Kim, D.; Choi, K. J.; Park, J.-G.; Hong, S.-H. *Cryst. Growth Des.* **2010**, *10*, 4746.
(51) Chen, Y. J.; Xue, X. Y.; Wang, Y. G.; Wang, T. H. *Appl. Phys. Lett.* **2005**, *87*, 233503.
(52) Fan, C.; Song, X.; Yin, Z.; Yu, H.; Sun, S. *J. Mater. Sci.* **2006**, *41*, 5696.
(53) Qin, L.; Xu, J.; Dong, X.; Pan, Q.; Cheng, Z.; Xiang, Q.; Li, F. *Nanotechnology* **2008**, *19*, 185705.
(54) Cheng, B.; Russell, J. M.; Shi, W.; Zhang, L.; Samulski, E. T. *J. Am. Chem. Soc.* **2004**, *126*, 5972.
(55) Jiang, X.; Wang, Y.; Herricks, T.; Xia, Y. *J. Mater. Chem.* **2004**, *14*, 695.
(56) Ba, J.; Polleux, J.; Antonietti, M.; Niederberger, M. *Adv. Mater.* **2005**, *17*, 2509.
(57) de Monredon, S.; Cellot, A.; Ribot, F.; Sanchez, C.; Armelao, L.; Gueneau, L.; Delattre, L. *J. Mater. Chem.* **2002**, *12*, 2396.
(58) Zhang, J.; Gao, L. *J. Solid State Chem.* **2004**, *177*, 1425.
(59) Wu, N.-L.; Wang, S.-Y.; Rusakova, I. A. *Science* **1999**, *285*, 1375.
(60) Huang, H.; Lee, Y. C.; Tan, O. K.; Zhou, W.; Peng, N.; Zhang, Q. *Nanotechnology* **2009**, *20*, 115501.
(61) Long, R.; Dai, Y.; Huang, B. *J. Phys. Chem. C* **2009**, *113*, 650.
(62) Sensato, F. R.; Custodio, R.; Longo, E.; Beltrán, A.; Andrés, J. *Catal. Today* **2003**, *85*, 145.
(63) Yu, X.; Li, C.; Tang, H.; Ling, Y.; Tang, T.-A.; Wu, Q.; Kong, J. *Comput. Mater. Sci.* **2010**, *49*, 430.
(64) Beltrán, A.; Andrés, J.; Sambrano, J. R.; Longo, E. *J. Phys. Chem. A* **2008**, *112*, 8943.
(65) Cassia-Santos, M. R.; Souza, A. G.; Soledade, L. E. B.; Varela, J. A.; Longo, E. *J. Therm. Anal. Calorim.* **2005**, *79*, 415.
(66) Harunsani, M. H.; Oropeza, F. E.; Palgrave, R. G.; Egdell, R. G. *Chem. Mater.* **2010**, *22*, 1551.
(67) Ma, Y.; Navrotsky, A. *J. Am. Ceram. Soc.* **2010**, *93*, 3432.
(68) Naidu, H. P.; Virkar, A. V. *J. Am. Ceram. Soc.* **1998**, *81*, 2176.
(69) Zhao, Y.; Liu, J.; Shi, L.; Yuan, S.; Fang, J.; Wang, Z.; Zhang, M. *Appl. Catal., B* **2010**, *100*, 68.
(70) Yu, J.; Liu, S.; Zhou, M. *J. Phys. Chem. C* **2008**, *112*, 2050.
(71) Cao, Y.; He, T.; Zhao, L.; Wang, E.; Yang, W.; Cao, Y. *J. Phys. Chem. C* **2009**, *113*, 18121.
(72) Sasikala, R.; Shirole, A.; Sudarsan, V.; Sakuntala, T.; Sudakar, C.; Naik, R.; Bharadwaj, S. R. *Int. J. Hydrogen Energy* **2009**, *34*, 3621.
(73) Asokan, K.; Park, J. Y.; Choi, S.; Chang, C.; Kim, S. S. *Nano Res.* **2010**, *3*, 256.
(74) Qi, B.; Wu, L.; Zhang, Y.; Zeng, Q.; Zhi, J. *J. Colloid Interface Sci.* **2010**, *345*, 181.
(75) Tao, N.; Zhao, J.; Guo, Y.; Jiang, Y.; Ding, X.; Wang, Z. *Mater. Chem. Phys.* **2004**, *84*, 58.
(76) Wojdyr, M. *J. Appl. Crystallogr.* **2010**, *43*, 1126.
(77) Massiot, D.; Fayon, F.; Capron, M.; King, I.; Le Calvé, S.; Alonso, B.; Durand, J.-O.; Bujoli, B.; Gan, Z.; Hoatson, G. *Magn. Reson. Chem.* **2002**, *40*, 70.
(78) Cozzoli, P. D.; Kornowski, A.; Weller, H. *J. Am. Chem. Soc.* **2003**, *125*, 14539.
(79) Zhang, Z. H.; Zhong, X. H.; Liu, S. H.; Li, D. F.; Han, M. Y. *Angew. Chem., Int. Ed.* **2005**, *44*, 3466.
(80) Zhou, M.; Yu, J.; Liu, S.; Zhai, P.; Jiang, L. *J. Hazard. Mater.* **2008**, *154*, 1141.
(81) Mittemeijer, E. J.; Scardi, P. *Diffraction Analysis of the Microstructure of Materials*; Springer: Berlin, 2004; pp 1−14.
(82) Riwotzki, K.; Meyssamy, H.; Kornowski, A.; Haase, M. *J. Phys. Chem. B* **2000**, *104*, 2824.
(83) Soler-Illia, G. J. d. A. A.; Scolan, E.; Louis, A.; Albouy, P.-A.; Sanchez, C. *New J. Chem.* **2001**, *25*, 156.
(84) Yoldas, B. E. *J. Mater. Sci.* **1986**, *21*, 1087.
(85) Jenkins, R.; Snyder, R. L. *Introduction to X-ray Powder Diffractometry*; Wiley-Interscience: New York, 1996; pp 41−43.
(86) Castellanos, M.; West, A. R. *J. Chem. Soc., Faraday Trans. 1* **1980**, *76*, 2159.
(87) Chizmeshya, A. V. G.; Bauer, M. R.; Kouvetakis, J. *Chem. Mater.* **2003**, *15*, 2511.
(88) Ganguly, P.; Shah, N.; Phadke, M.; Ramaswamy, V.; Mulla, I. S. *Phys. Rev. B: Condens. Matter* **1993**, *47*, 991.
(89) Sayılkan, F.; Asiltürk, M.; Tatar, P.; Kiraz, N.; Arpaç, E.; Sayılkan, H. *J. Hazard. Mater.* **2007**, *148*, 735.
(90) Smith, D. L. *Thin Film Deposition: Principles and Practices*; McGraw-Hill Professional: New York, 1995; pp 223.
(91) Peng, X.; Schlamp, M. C.; Kadavanich, A. V.; Alivisatos, A. P. *J. Am. Chem. Soc.* **1997**, *119*, 7019.
(92) Mekis, I.; Talapin, D. V.; Kornowski, A.; Haase, M.; Weller, H. *J. Phys. Chem. B* **2003**, *107*, 7454.
(93) Steckel, J. S.; Zimmer, J. P.; Coe-Sullivan, S.; Stott, N. E.; Bulović, V.; Bawendi, M. G. *Angew. Chem., Int. Ed.* **2004**, *43*, 2154.
(94) Dabbousi, B. O.; Rodriguez-Viejo, J.; Mikulec, F. V.; Heine, J. R.; Mattoussi, H.; Ober, R.; Jensen, K. F.; Bawendi, M. G. *J. Phys. Chem. B* **1997**, *101*, 9463.
(95) Cao, Y.; Banin, U. *J. Am. Chem. Soc.* **2000**, *122*, 9692.
(96) Ghosh, P.; Oliva, J.; De la Rosa, E.; Haldar, K. K.; Solis, D.; Patra, A. *J. Phys. Chem. C* **2008**, *112*, 9650.
(97) Kulshreshtha, S. K.; Sasikala, R.; Sudarsan, V. *J. Mater. Chem.* **2001**, *11*, 930.
(98) Lee, E. J. H.; Ribeiro, C.; Longo, E.; Leite, E. R. *J. Phys. Chem. B* **2005**, *109*, 20842.
(99) In an attempt to confirm the core/shell structure, we performed EDX line scans for single particles on a FEI-Titan 80−300 TEM. However, these ligand-protected particles lacked the necessary stability under the 300 keV beam to collect EDX data sufficient to extract meaningful and reproducible analyses
(100) Ranade, M. R.; Navrotsky, A.; Zhang, H. Z.; Banfield, J. F.; Elder, S. H.; Zaban, A.; Borse, P. H.; Kulkarni, S. K.; Doran, G. S.; Whitfield, H. J. *Proc. Natl. Acad. Sci. U.S.A.* **2002**, *99*, 6476.
(101) Bryan, J. D.; Gamelin, D. R. *Doped Semiconductor Nanocrystals: Synthesis, Characterization, Physical Properties, and Applications*; John Wiley & Sons, Inc.: New York, 2005; pp 47−126.